





# Adaptive Active Damping-Based Grid-side Current Harmonic Suppression Method for Totem-pole Bridgeless PFC Converter

Binxing Li , Gaolin Wang , Yujia Zhu, Guoqiang Zhang , Dianguo Xu   
Harbin Institute of Technology, China

Corresponding author: Gaolin Wang, WGL818@hit.edu.cn

Speaker: Binxing Li, LBX@hit.edu.cn

## Abstract

In order to broaden the adaptation range of the conventional fixed active damping grid-side current harmonic suppression method, an adaptive active damping-based grid-side current harmonic suppression method is proposed in this paper. Besides, the totem-pole bridgeless PFC converter input impedance characteristics and Hermite interpolation-based active damping method are theoretically analyzed. Finally, the proposed method is validated on a 1.5 kW GaN totem-pole bridgeless PFC converter.

## 1 Introduction

Currently, GaN devices as wide-bandgap semiconductors have been widely used in the field of high-performance converters. Totem pole bridgeless PFC converters based on GaN devices have the advantages of high efficiency, high switching frequency, and high power density compared to Boost PFC converters, which can significantly improve the system performance [1,2]. In practical applications, due to the impact of loads and transmission lines, the grid voltage contains certain harmonic components. These harmonics are converted into harmonic currents by the converter [3]. Due to the influence of system LC resonance, the amplitude of grid-side current harmonics increases, thereby affecting the grid-side power quality [4]. Therefore, grid-side current harmonics are an important issue in the application of totem-pole bridgeless PFC converters and have attracted widespread attention.

The primary measures to mitigate grid-side current harmonics include two main approaches: harmonic compensation methods based on nonlinear control strategies and harmonic suppression methods based on active damping. Harmonic compensation methods based on nonlinear control strategies suppress current harmonics by adjusting the gain of the controller at harmonic frequencies. However, the design of such controllers is relatively complex [5].

Active damping methods can primarily be categorized into two types from a control perspective: the addition of digital filters in the forward path [6] and the addition of state variable feedback [7]. The method involving the addition of digital filters in the forward path is essentially a series compensation method. By integrating the filter's transfer function in a cascaded manner into the control loop, it adjusts the open-loop gain-frequency or

phase-frequency characteristics to achieve harmonic suppression. In practical applications, the parameters for active damping based on series compensation are difficult to design accurately due to the influence of system impedance and other factors. Its performance is overly dependent on the filter parameters, and when the resonance frequency shifts, the effectiveness of the digital filter-based damping scheme diminishes.

The active damping method based on additional state variable feedback achieves active damping control by constructing virtual admittance and utilizing state variable feedback, thereby altering the system's frequency characteristics to suppress current harmonics. However, the parameters of the virtual impedance in such methods depend on the system model, and the suppression effect deteriorates when the system impedance changes or the power range is wide [8].

Three main methods are used to improve the adaptability of active damping strategies: damping adjustment, adaptive methods, and damping optimization. Adjusting the amplitude and phase of virtual admittance can achieve the widest load adaptation range. In [9], the system impedance model under different loads is used to determine the range of virtual admittance (amplitude and phase) that meets the requirements, from which effective virtual admittance for suppressing current harmonics over a wide load range is selected. However, this method cannot cover the entire power range, and the harmonic suppression effect is poor at the edge of the effective range. Additionally, using the damping optimization method can effectively reduce harmonics. In [10], active damping is automatically adjusted based on the feedback of the current harmonic variation trend until optimal harmonic suppression is achieved. However, this method has a slow convergence rate and is less effective in tracking fluctuating loads.

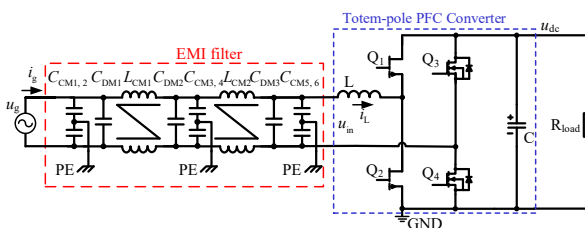
Adaptive algorithms can effectively suppress current harmonics. The Model Reference Adaptive System (MRAS) algorithm can estimate the current system damping to obtain the optimal virtual admittance. However, there is a risk of non-convergence during parameter adjustment, which may prevent achieving the desired effect. In [11], an adaptive extended Kalman filter combined with an adaptive passive controller was designed to eliminate instability issues in DC microgrid buck converters considering constant power loads. However, the tracking accuracy is limited by the model's accuracy. In [12], a cubic spline interpolation method was used to establish an equivalent circuit model for a DC-DC converter with a load-variable noise source, achieving better consistency compared to the waveform decomposition method. It also reduces the frequency of repetitive parameter identification when the load changes. Further research is needed to reduce the complexity of control strategies and enhance adaptability under different load conditions.

A novel method for suppressing grid-side current harmonics based on Hermite interpolation adaptive active damping is proposed in this paper. A system impedance model is established, and a virtual admittance matrix is constructed. The Hermite interpolation method is used to map the relationship between virtual admittance and power, achieving harmonic suppression over a wide load range. The effectiveness and adaptability of the proposed method under different load conditions are verified through experimental results.

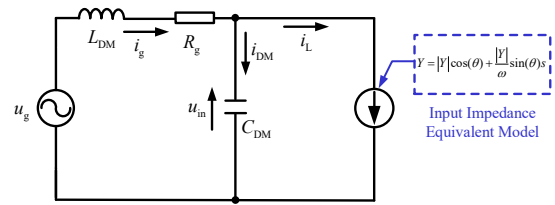
## 2 Proposed Adaptive Active Damping-Based Harmonic Suppression Method

### 2.1 Analysis of Input Impedance Characteristics of PFC Converters

The totem-pole bridgeless PFC converter topology is shown in **Fig. 1(a)**, where the PFC converter contains a two-stage EMI filter. The common mode inductance and common mode capacitance have a negligible effect on the input current. Since the differential mode capacitance and differential mode inductance in the EMI filter will generate LC resonance, when the converter is connected to the grid, it will amplify the current harmonics around the resonance frequency and introduce them into the grid-side current. The equivalent circuit of the converter can be obtained as shown in **Fig. 1(b)**. Where



(a)



(b)

**Fig. 1.** Topology and equivalent model of the totem-pole bridgeless PFC converter. (a) Topology circuit. (b) Equivalent model.

$Y$  is the converter input conductance,  $L_{DM}$  and  $C_{DM}$  are the equivalent differential mode inductance and differential mode capacitance, respectively.

According to **Fig.1(b)** and reference [9], the system admittance can be expressed as

$$Y_g(s) = \frac{I_g(s)}{U_g(s)} = \frac{Y(s) + Y_{DM}(s)}{[Y(s) + Y_{DM}(s)](L_{DM}s + R_g) + 1} \quad (1)$$

where  $Y_{DM}(s) = sC_{DM}$ . the totem-pole PFC converter input conductance  $Y(s)$  can be expressed as the ratio of the inductor current to the converter input voltage

$$Y(s) = \frac{I_L(s)}{U_{in}(s)} = Y_1(s) + Y_2(s) \quad (2)$$

where

$$\begin{cases} Y_1(s) = \frac{g_{in} K_{ib} G_{ic} G_{id} e^{-T_d s}}{V_m (1 + T_i)} \\ Y_2(s) = \frac{G_{iv}}{1 + T_i} \end{cases} \quad (3)$$

$g_{in}$ ,  $T_d$ , and  $K_{ib}$  are the input admittance, the system delay, and the reciprocal of the current base value, respectively.  $G_{iv}$ ,  $G_{id}$ , and  $T_i$  are the transfer function between  $I_L(s)$  and  $U_{in}(s)$ , the transfer function between  $I_L(s)$  and  $D(s)$ , and the loop gain transfer function, respectively.  $G_{ic}$  is the current regulator and  $V_m$  is the PWM Gain.

**Fig. 2** shows the Bode diagrams of system admittance under different loads, with the current loop bandwidth

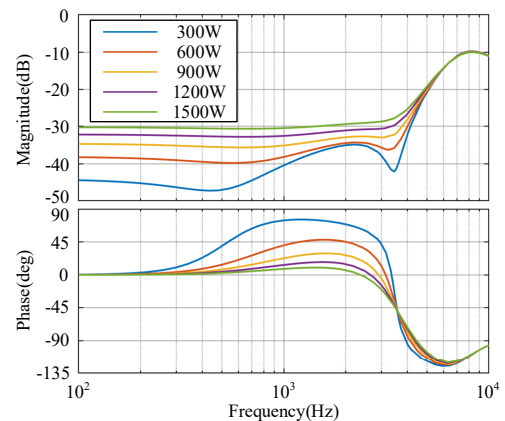


**Fig. 2.** Bode diagrams of system admittance under different loads.

set to 500Hz. It can be observed that both the magnitude and phase of the admittance at harmonic frequencies vary with the load power. Therefore, it is necessary to develop an adaptive active damping harmonic suppression method to achieve effective harmonic suppression across a wide load range.

## 2.2 Adaptive active damping method

The control block diagram of the GaN totem-pole bridgeless PFC converter based on adaptive active damping is shown in **Fig. 3**. In order to suppress the grid-side current harmonics,  $u_{in}$  is filtered to obtain the harmonic voltage, and the current reference component is calculated by virtual conduction. In addition, active damping is assigned considering the bandwidth limitation of the current controller. Active damping control is realized by modulating the voltage component and the reference current component to change the inductor current and suppress the harmonic currents. The virtual admittance used in this method can be adaptively adjusted based on power, effectively reducing grid-side current harmonics over a wide load range.

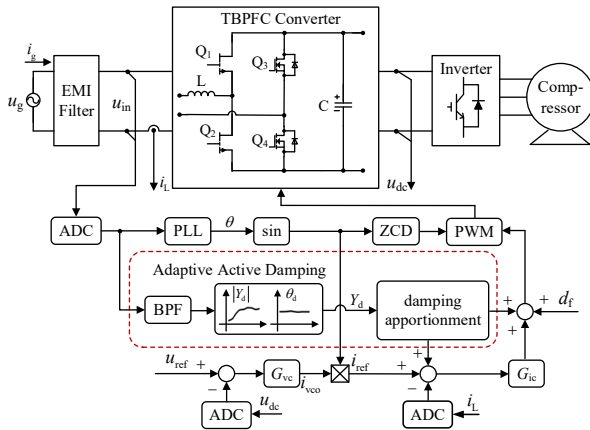


**Fig. 3.** Block diagram of totem-pole bridgeless PFC converter with the adaptive active damping control.

Matching the system impedance at the target harmonic frequency ( $\omega_d$ ) using virtual conductance. According to (1), the transfer function of the system at  $\omega_d$  is

$$Y_{g\_d}(s) = \frac{i_{g\_d}(s)}{u_{g\_d}(s)} = \frac{Y(s) + Y_{DM}(s) + Y_d(s)}{[Y(s) + Y_{DM}(s) + Y_d(s)](L_{DM}s + R_g) + 1} \quad (4)$$

where  $i_{g\_d}(s)$ ,  $u_{g\_d}(s)$ , and  $Y_d(s)$  are the grid-side harmonic current enabling active damping, grid-side harmonic voltage, and virtual admittance at  $\omega_d$ , respectively.  $Y_d(s)$  can be expressed as

$$Y_d = |Y_d| \cos \theta_d + \frac{|Y_d|}{\omega_d} \sin \theta_d s \quad (5)$$

where  $|Y_d|$  and  $\theta_d$  are the magnitude and phase of  $Y_d$ .

A three-dimensional graph is plotted with  $|Y_d|$  as the x-axis,  $\theta_d$  as the y-axis, and  $|Y_{g\_d}|$  as the z-axis. The angle and admittance are described in the form of per-unit values. The angle base value is  $\pi$  rad and the admittance base value is 0.04 S. The lowest point on the three-dimensional graph represents the minimum system admittance obtained after applying virtual admittance compensation under the current power condition, corresponding to the optimal virtual admittance point. Taking a load power of 900W as an example, the optimal virtual admittance point at 900W is determined to be (0.42, -0.9, -72.04), as shown in **Fig. 4**. Similarly, results for other load powers can be obtained, illustrating the range of virtual admittance satisfying harmonic standards and the optimal virtual admittance points, as shown in **Fig. 5**. It is observed that both the magnitude and phase of the virtual admittance vary with load power. To accurately consider the impact of system nonlinearity on active damping, it is necessary to obtain the magnitude and phase of admittance at different powers. As the admittance corresponds to the system's state, dependent on load power, traditional methods increase sampling data as much as possible to obtain a continuous virtual admittance curve, which is time-consuming and computationally intensive. To address this issue, a data sampling and curve fitting algorithm based on Hermite interpolation is employed, requiring only a small amount of sampling data to form a continuous virtual admittance curve.

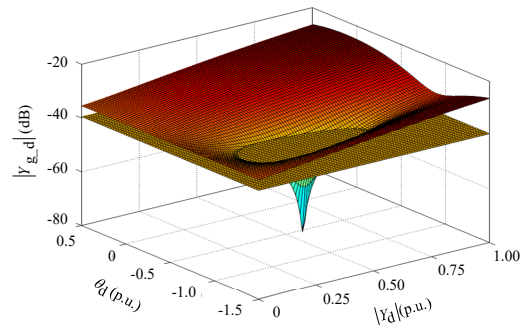


**Fig. 4.** System admittance results at 900W with different virtual admittances.

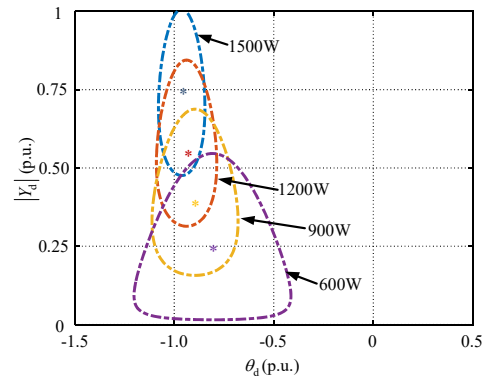


**Fig. 5.** Optimum virtual admittance values under different power loads.

### 2.3 Hermite-based adaptive active damping realization

In order to ensure that the interpolation function approximates the interpolated function more effectively, the Hermite interpolation method not only requires "passing through points" meaning that the interpolation function matches the interpolated function at the nodes but also requires that they have the same first derivative at all or some of the nodes. However, when performing high-order interpolation over a wide range, the approximation effect is often not ideal, so segmented low-order interpolation is generally used. Additionally, because the derivative of the piecewise linear interpolation function at the nodes often does not exist, resulting in poor smoothness, segmented cubic Hermite interpolation is employed.

The optimal virtual admittance magnitude and phase corresponding to different powers are interpolated. Upon comparison, for the data of  $|Y_d|$  and  $\theta_d$ , situations arise where the ordinate of adjacent data points is nearly equal. In such cases, using the pchip interpolation method, namely the segmented cubic Hermite interpolation polynomial method, is more suitable. This method helps avoid overshoot and allows for more accurate connection of plateau regions.

Set  $\theta_d = f(P)$  be a function with a value  $\theta_{dj} = f(P_j)$  and a derivative value  $m_j = f'(P_j)$  ( $j = 0, 1, \dots, n$ ) at node  $a = P_0 < P_1 < P_2 < \dots < P_n = b$ . A segmented cubic Hermite interpolation function  $L_h(P)$  can be constructed to satisfy the following three conditions:

- (1)  $L_h \in C^1[a, b]$ ;
- (2)  $L_h(P_j) = \theta_{dj}, L'_h(P_j) = m_j, j = 0, 1, \dots, n$ ;
- (3)  $L_h(P)$  is a cubic polynomial on each interval  $[P_j, P_{j+1}]$ .

After the operation, the expression of  $L_h(P)$  is written as

$$\begin{aligned}
 L_h(P) = & \left(1 + 2 \frac{P - P_j}{P_{j+1} - P_j}\right) \left(\frac{P - P_{j+1}}{P_j - P_{j+1}}\right)^2 \theta_{dj} \\
 & + \left(1 + 2 \frac{P - P_{j+1}}{P_j - P_{j+1}}\right) \left(\frac{P - P_j}{P_{j+1} - P_j}\right)^2 \theta_{dj+1} \\
 & + (P - P_j) \left(\frac{P - P_{j+1}}{P_j - P_{j+1}}\right)^2 m_j \\
 & + (P - P_{j+1}) \left(\frac{P - P_j}{P_{j+1} - P_j}\right)^2 m_{j+1}
 \end{aligned} \quad (6)$$

where  $P \in [P_j, P_{j+1}]$ .

The virtual admittance at the selected frequency point of 850Hz is obtained based on the system model. Subsequently, the Hermite interpolation method mentioned above is employed to respectively interpolate and fit the magnitude and phase of the virtual admittance, resulting in fitting functions for both magnitude and phase.

The conformity between the fitting results and the sampling points is depicted in Fig. 6, illustrating a satisfactory fitting effect for both magnitude and phase.

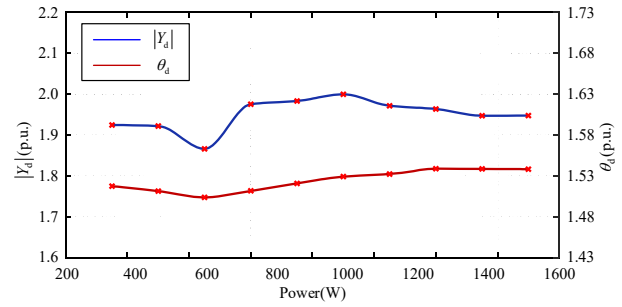


Fig. 6. Virtual conductance magnitude and phase interpolation fitting results.

### 3 Experimental Results

The experimental platform for the totem-pole bridgeless PFC converter, as depicted in Fig. 7, employs a compressor drive system as the load, with load adjustments made by varying the compressor speed. The main parameters of the totem-pole bridgeless PFC converter are presented in Table 1, with a rated load of 1500W.

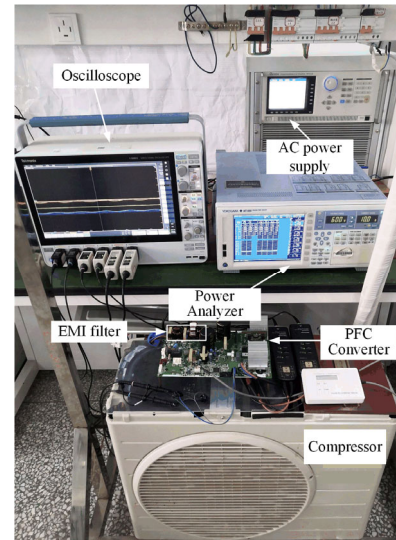
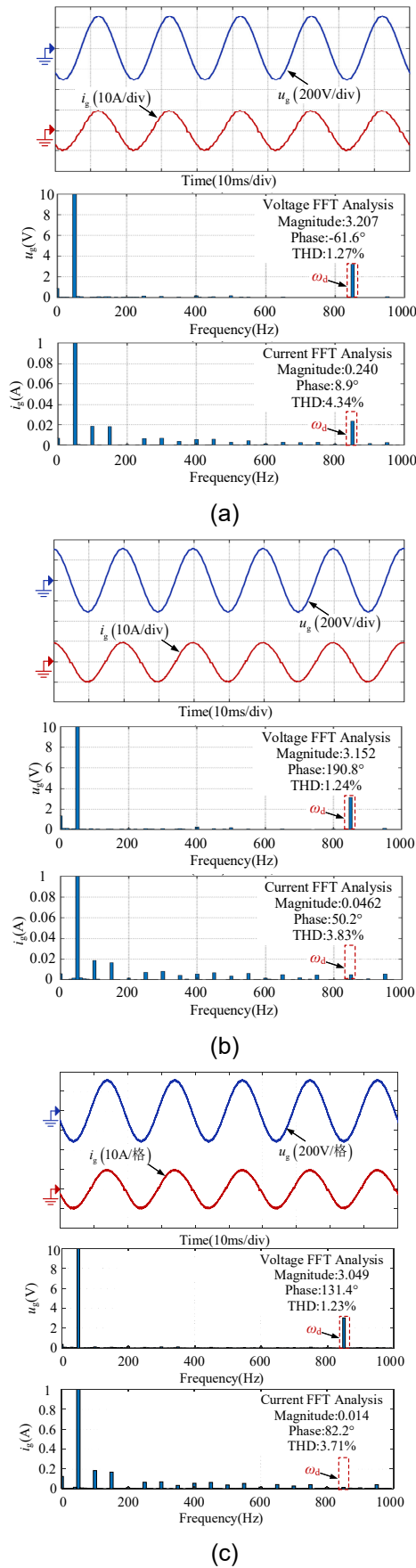


Fig. 7. Experimental platform of totem-pole bridgeless PFC converter.

Table 1  
Totem-pole Bridgeless PFC Converter Parameters

| Parameters                   | Value |
|------------------------------|-------|
| Rated power (W)              | 1500  |
| Switching frequency (kHz)    | 150   |
| Control frequency (kHz)      | 50    |
| Grid frequency (Hz)          | 50    |
| Boost inductance (μH)        | 500   |
| DC-link capacitance (μF)     | 940   |
| Differential capacitance(μF) | 4     |
| Differential inductance(μH)  | 80    |
| Common mode capacitance(nF)  | 5.1   |
| Common mode inductance(mH)   | 4     |





**Fig. 8.** Experimental results at 1500 W. (a) Without active damping. (b) With fixed active damping. (c) With adaptive active damping.

The experimental results at rated load are shown in **Fig. 8**, where the waveforms in subfigures (a), (b), and (c) are the waveforms before and after the current harmonic suppression strategy enabled, and the waveforms with the adaptive strategy, respectively. It can be seen that the current harmonic at  $\omega_d$  reaches 0.4 A without enabling the current harmonic suppression strategy. After enabling the fixed virtual conductor harmonic suppression strategy, the current harmonic decreases to 0.046 A. When the adaptive active damping is further adopted, the current harmonic further decreases to 0.014 A, and the current harmonic suppression effect is significant. The THD of the grid-side current decreases by 0.63%, indicating that the proposed algorithm does not introduce significant harmonics at other frequencies, which is conducive to further improving the performance of the grid-side current.

In order to evaluate the adaptability of the adaptive active damping harmonic suppression method, experiments are carried out at different power loading conditions, and the harmonic test results are shown in **Fig. 9**. It can be seen that the proposed method is well adapted within the range of 300W-1500W, and the suppression effect is further improved in comparison with that of the fixed virtual conductor method.

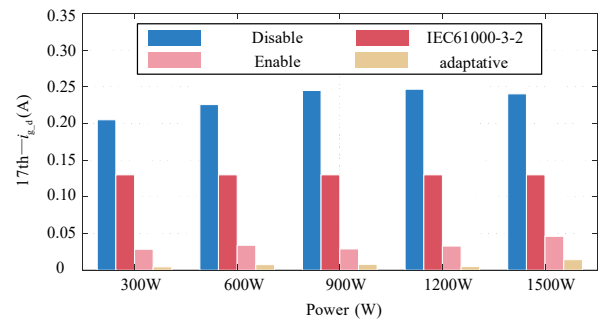


**Fig. 9.** Comparison of grid-side current performance before and after applying harmonic suppression algorithm at different load conditions.

## 4 Conclusion

For the grid-side current harmonics caused by LC resonance, a grid-side current harmonic suppression method based on adaptive active damping has been proposed in this paper, which utilizes a digital filter to extract the input voltage harmonics and an interpolation method to design an adaptive virtual conductor. The accuracy and adaptability of the damping control are improved. Experimental results have demonstrated that the investigated current harmonic suppression method can improve the grid-side power quality over a wide load range.

## 5 References

- [1] Q. Huang, R. Yu, Q. Ma, and A. Q. Huang, "Predictive ZVS control with improved ZVS time margin and limited variable frequency range for a 99%

- efficient, 130-W/in<sup>3</sup> MHz GaN totem-pole PFC rectifier,” *IEEE Trans. Power Electron.*, vol. 34, no. 7, pp. 7079-7091, July 2019.
- [2] Y. Jia, H. Wu, L. Yang, X. Xu, Y. Liu, F. Yang, and Y. Xing, “Characterization and optimal control of totem-pole PFC converter with high frequency GaN HEMTs and low frequency Si diodes,” *IEEE Trans. Ind. Electron.*, vol. 68, no. 11, pp. 10740-10749, Nov. 2021.
- [3] H. S. Nair, and N. L. Narasamma, “An improved digital algorithm for boost PFC converter operating in mixed conduction mode,” *IEEE J. Emerg. Sel. Top. Power Electron.*, vol. 8, no. 4, pp. 4235-4245, Dec. 2020.
- [4] B. Li, D. Ding, Q. Wang, G. Zhang, G. Wang, and D. Xu, “Virtual admittance reshaping based input current phase shift suppression method for totem-pole bridgeless PFC converter,” *IEEE Trans. Power Electron.*, vol. 38, no. 3, pp. 2925-2939, March 2023.
- [5] P. Cui, and G. Zhang, “Modified repetitive control for odd-harmonic current suppression in magnetically suspended rotor systems,” *IEEE Trans. Ind. Electron.*, vol. 66, no. 10, pp. 8008-8018, Oct. 2019.
- [6] S. Chen, and Y. Ye, “Robust  $H^\infty$  Active Damping Filter With Preserved Resonant Peak for Resonant Harmonic Suppression,” *IEEE J. Emerg. Sel. Top. Power Electron.*, vol. 12, no. 3, pp. 2580-2591, 2024.
- [7] X. Huang, X. Ruan, L. Zhang, and F. Liu, “Second harmonic current reduction schemes for DC–DC converter in two-stage PFC converters,” *IEEE Trans. Power Electron.*, vol. 37, no. 1, pp. 332-343, Jan. 2022.
- [8] K. Ji, H. Pang, Z. He, Y. Li, D. Liu, and G. Tang, “Active/passive method-based hybrid high-frequency damping design for MMCs,” *IEEE J. Emerg. Sel. Top. Power Electron.*, vol. 9, no. 5, pp. 6086-6098, Oct. 2021.
- [9] B. Li, D. Ding, Q. Wang, G. Zhang, B. Fu, G. Wang, and D. Xu, “Input voltage feedforward active damping-based input current harmonic suppression method for totem-pole bridgeless PFC converter,” *IEEE J. Emerg. Sel. Top. Power Electron.*, vol. 11, no. 1, pp. 602-614, Feb. 2023.
- [10] Z. Ren, D. Ding, G. Wang, B. Li, Q. Wang, G. Zhang, and D. Xu, “Adaptive Virtual Admittance Reshaping-Based Resonance Suppression Strategy for PMSM Drives With Small DC-Link Capacitor,” *IEEE Trans. Power Electron.*, vol. 39, no. 3, pp. 3109-3121, 2024.
- [11] M. Abdolahi, J. Adabi, and S. Y. M. Mousavi, “An Adaptive Extended Kalman Filter With Passivity-Based Control for DC-DC Converter in DC Microgrids Supplying Constant Power Loads,” *IEEE Trans. Ind. Electron.*, vol. 71, no. 5, pp. 4873-4882, 2024.
- [12] S. Zhang, K. Iokibe, and Y. Toyota, “A Load-variable Noise-source Equivalent Circuit Model for DC-DC Converter Considering Cubic Spline Interpolation,” in *2022 IEEE CPMT Symposium Japan (ICSJ)*, 2022, pp. 154-157.